

In situ decoration of plasmonic Au nanoparticles on graphene quantum dots-graphitic carbon nitride hybrid and evaluation of its visible light photocatalytic performance

This content has been downloaded from IOPscience. Please scroll down to see the full text.

2017 Nanotechnology 28 395703

(<http://iopscience.iop.org/0957-4484/28/39/395703>)

View [the table of contents for this issue](#), or go to the [journal homepage](#) for more

Download details:

IP Address: 14.139.221.122

This content was downloaded on 06/09/2017 at 10:53

Please note that [terms and conditions apply](#).



NANORAMAN: Multi Technique Analysis
Platform from **MACRO** to **NANOSCALE**

[Learn more >>](#)

HORIBA
Scientific

In situ decoration of plasmonic Au nanoparticles on graphene quantum dots-graphitic carbon nitride hybrid and evaluation of its visible light photocatalytic performance

Gone Rajender¹, Biswajit Choudhury² and P K Giri¹

¹Department of Physics, Indian Institute of Technology Guwahati, Guwahati 39, India

²Physical Sciences Division, Institute of Advanced Study in Science and Technology, Paschim Borigaon, Guwahati 35, India

E-mail: biswa.tezu@gmail.com

Received 6 June 2017, revised 5 July 2017

Accepted for publication 20 July 2017

Published 6 September 2017



Abstract

This work spotlights the development of a plasmonic photocatalyst showing surface plasmon induced enhanced visible light photocatalytic (PC) performance. Plasmonic Au nanoparticles (NPs) are decorated over the hybrid nanosystem of graphitic carbon nitride (GCN) and graphene quantum dots (GQD) by citrate reduction method. Surface plasmon resonance (SPR) induced enhancement of Raman G and 2D band intensity is encountered on excitation of the Plasmonic hybrid at 514.5 nm, which is near to the 532 nm absorption band of Au NPs. Time-resolved photoluminescence and XPS studies show charge transfer interaction between GQD-GCN and Au NPs. Plasmonic hybrid exhibits an enhanced PC activity over the other catalysts in the photodegradation of methylene blue (MB) under visible light illumination. Plasmonic photocatalyst displays more than 6 fold enhancement in the photodecomposition rate of MB over GQD and nearly 2 fold improvement over GCN and GQD-GCN. GQD-GCN absorbs mostly in the near visible region and can be photoexcited by visible light of wavelength (λ) < 460 nm. Plasmon activation in Au NPs decorated GQD-GCN could exploit the entire UV-visible light for photocatalysis. Furthermore, plasmonic Au act as antennas for accumulation and enhancement of localized electromagnetic field at the interface with GQD-GCN, and thereby promotes photogeneration of large numbers of carriers on GQD-GCN. The carriers are separated by charge transfer migration from hybrid to Au NPs. Finally, the carriers on the plasmonic Au nanostructures initiate MB degradation under visible light. Our results have shown that plasmon decoration is a suitable strategy to design a carbon based hybrid photocatalyst for solar energy conversion.

Keywords: luminescence, optical, colloid

(Some figures may appear in colour only in the online journal)

1. Introduction

Conversion of solar energy into chemical energy with the aid of photocatalysis is considered to be a promising approach to

produce clean, sustainable energy and for the degradation of environmental pollutants [1–3]. Semiconductor metal oxides (SMOs) have long been studied as an excellent photocatalytic (PC) material in water splitting and degradation of organic

dyes [1–4]. These wide band gap SMO nanostructures are active photocatalysts under UV light but inefficient to utilize visible light for photocatalysis. By incorporation of metal and non-metal dopants, SMO is made efficient absorber of visible light [5–8]. However, dopant inhomogeneity and dopants acting as carrier recombination centres are the major hurdles in their effectiveness as a photocatalyst. Recently, carbon based 2D nanomaterials, viz. graphene and graphitic carbon nitride (GCN), have gained sufficient attentions in the field of photocatalysis, energy storage, sensing, etc [9–13]. Unlike gapless metallic graphene oxygenated functional groups in graphene oxide (GO) helps in the opening up of a band gap in the system. The hydrophilic functionalities also help graphene to form a stable dispersion in aqueous system [14]. Ramirez *et al* reported efficient removal of phenol and 4-chlorophenol from contaminated water using graphite oxide and GOs as photocatalysts [15, 16]. In another study, Shan *et al* reported enhanced tylosin degradation in a composite system of GO with goethite [17]. Graphitic carbon nitride (g-C₃N₄), having a band gap of 2.7 eV is another suitable material for H₂ production as the water oxidation-reduction potential appears in the band gap [13, 18]. These carbon-based 2D materials are excellent carriers of electrons but suffer from poor absorption of visible light and fast recombination of photoexcited carriers.

Hybrid nanostructures of carbon based materials with SMO are reported to exhibit superior PC activity than those of their parent counterparts [19, 20]. However, developing a good interfacial contact between the two systems is a vital step for efficient charge carrier separation at the interface. More recently, nanohybrid systems composed of 2D–2D carbon nanostructures are drawing attention as a material for photocatalysis under visible light [21, 22]. This hybrid system is stabilized through π – π van der Waal interaction. The carriers in 2D materials have shorter diffusion length. Thus, easy carrier migration from bulk to surface is facilitated and because of the energy offset between valence and conduction band of the constructed hybrid components the photo-generated charge carriers are efficiently separated [21]. Coupled systems of g-C₃N₄ and GO are reported to show enhanced PC activity. The oxygenated functional groups can tune the optoelectronic properties of the hybrid system making it suitable for photocatalysis [22–24]. In a recent study, researchers observed improved PC activity in graphene quantum dots (GQDs) decorated graphitic carbon nitride (GCN) [25, 26]. In a theoretical study, Ma *et al* observed strong interfacial electron coupling when GQD is hybridized with GCN [25]. This facilitates charge carrier separation at the interface making the hybrid a better photocatalyst. In another study, Zou *et al* reported improved H₂ generation over GQD decorated C₃N₄ nanosheets [26].

In the present study, we have developed a 0D–2D hybrid nanosystem of GQDs and GCN. Unlike pristine GQD and GCN which show absorption in the UV region, GQD-GCN shows absorption in the extended UV–visible region. It is shown that interfacial charge separation is much prolonged in GQD-GCN. However, because of the poor absorption of visible light this hybrid system is inefficient to utilize

maximal visible light for photocatalysis. Since plasmon absorption covers the entire UV–vis–NIR range of the solar spectrum, plasmon decoration over a hybrid catalyst could maximize the spectral range for visible light PC applications. Furthermore, plasmon activation promotes strong light intensity enhancement at the interface of Au with GQD-GCN and thereby, facilitates carrier separation and migration from GQD to GCN and finally to Au nanoparticles (NPs).

Thus, integration of Au NPs with GQD-GCN has endowed the plasmonic hybrid photocatalyst with improved PC performance in the degradation of methylene blue (MB) by the utilization of localized surface plasmon resonance (SPR) of Au NPs [27–29].

2. Experimental details

2.1. Preparation of g-C₃N₄ (GCN)

GCN was prepared using urea as the starting precursor. 10 g of urea was taken in a silica crucible and covered with a lid. The crucible was subjected to heat treatment at 550 °C for 3 h at a heating rate of 5°/min. The crucible was taken out of the furnace when the temperature had reached room temperature. The product was pale yellow in colour. The corresponding g-C₃N₄ sample was labelled as GCN.

2.1.1. Synthesis of GQDs. GO was synthesized by a modified Hummers method, as reported elsewhere [30]. Typically, the as-synthesised GO sheets were oxidized with concentrated H₂SO₄ and HNO₃ mixture (volume ratio 1:3) with 1 mg of GO. The resulting product was referred to as oxidized GO (OGO). For the synthesis of GQDs, the OGO was used as precursor material and dimethyl formamide (DMF) as the solvent. OGO was mixed with (1 mg/0.1 ml) of DMF and ultrasonicated for a few minutes to obtain the uniform dispersion. Further, this solution was transferred into a Teflon lined autoclave (100 ml) and heated at 200 °C for 7 h.

2.1.2. Preparation of GQD-GCN hybrid system. For the preparation of a GQD-GCN hybrid system, equal weight ratio of GQD and GCN (1:1) was taken and added to 100 ml water in two separate beakers. Both beakers were kept for ultrasonic treatment for 1 h to allow complete dispersion in water. GCN solution was kept in stirring condition. After 15 min, the GQDs was added to the GCN solution and the mixture was stirred for another 1 h. After completion of stirring, the mixture was centrifuged and dried at 60 °C in a hot air oven to collect the dried product.

2.1.3. Synthesis of Au NPs. Au NPs were prepared by a citrate reduction method [31]. Typically, 0.5 mM gold (III) chloride was prepared in 300 ml water and heated to boiling. 30 ml of 0.1 M trisodium citrate dihydrate (TSC) was added to the boiling gold chloride solution with continuous monitoring of colour changing. When the colour of the solution became purple red, the reaction was immediately

stopped and cooled down to room temperature. This gave rise to the colloidal Au NPs.

2.1.4. Decoration of Au NPs on GQD-GCN. *In situ* decoration of Au NPs over GQD-GCN was performed by directly adding the hybrid catalyst GQD-GCN in the gold chloride solution. GQD to GCN weight ratio was 1:1 and the concentration of gold chloride solution was 0.5 mM. Typically, 30 mg of GQD-GCN was taken in 300 ml of double distilled water in a 500 ml beaker and subjected to ultrasonication for 30 min. The large volume of water was taken for better dispersion of GQD-GCN and to prevent agglomeration of Au NPs over the hybrid nanosystem. The solution containing GQD-GCN was then heated at 90 °C. 30 ml of 38.8 mM TSC was added dropwise to the gold solution containing GQD-GCN. After 30 min of stirring, the final mixture got a purple-white colour. At this point, the reaction was immediately stopped and cooled down to room temperature. The solution was centrifuged three times with water and then dried at 60 °C. The obtained product was Au NPs decorated over GQD-GCN hybrid and named as Au@GQD-GCN.

2.2. Characterisation techniques

Phase structure of the as prepared samples was characterized with x-ray diffraction (Rigaku RINT 2500 TTRAX-III). The XRD pattern was obtained by exciting the samples with Cu K α x-ray radiation ($\lambda = 1.54 \text{ \AA}$) at a scanning rate of 5°/min and within the scanning range of 8°–70°. Morphology and particle sizes were observed in transmission electron microscope (JEOL JEM 2010, 200 kV). Field emission scanning electron micrograph (FESEM) images and elemental mapping were obtained in a scanning electron microscope (Sigma, Zeiss). Fourier transform infrared (FTIR) spectroscopy measurements were performed in Perkin Elmer, Spectrum BX spectrophotometer. Raman scattering measurements were performed in a Horiba Raman spectrometer (LabRam HR800, Jobin Yvon) at excitation wavelengths of 488 nm and 514.5 nm, respectively. X-ray photoelectron spectroscopy (XPS) measurements were performed in a PHI X-tool automated photoelectron spectrometer (ULVAC-PHI, Japan) with an Al K α x-ray beam source (1486.6 eV) and with a beam current of 20 mA. Absorption spectra were taken in UV–vis spectrophotometer (Perkin Elmer, UV win Lab). PL measurements were carried out by exciting the samples at 375 nm (Fluoromax-4, Horiba Scientific). Time-resolved PL (TRPL) spectra were recorded using a picosecond time-resolved luminescence spectrometer (FSP920, Edinburgh Instruments).

2.3. PC measurements

2.3.1. Photodegradation of MB. For the PC study, we have considered non-biodegradable MB dye as the model organic pollutant. PC experiment was performed by adding a small amount of catalyst (6 mg) to 100 ml aqueous MB solution with an initial MB concentration of 8 mg l⁻¹. Aqueous MB solution with catalyst was stirred in dark for 45 min in order

to obtain an equilibrium condition between dye and the catalyst. The solution was irradiated under visible light ($\lambda > 400 \text{ nm}$, 450 Watt Xe arc lamp, ORIEL instruments) with external UV cut off filter and mirror for beam reflection. During light irradiation cold water was circulated throughout the reactor to maintain the temperature of the system near room temperature. After every 15 min 1–2 ml of solution was taken and centrifuged. The irradiation was continued up to 180 min. Photodegradation of MB was monitored by the decrease of its absorption intensity (peak at 665 nm) with irradiation time.

2.3.2. Hydroxyl radical test. In a typical experiment, a solution was prepared with $2 \times 10^{-3} \text{ M}$ of NaOH and $5 \times 10^{-3} \text{ M}$ of terephthalic acid (TA) in 100 ml DI water [32]. After a few min of stirring 6 mg catalyst was added to the solution. The irradiation time and sample collection after each step of irradiation were similar to the above experiment. After completion of the irradiation experiment, small volume of TA was taken and its PL intensity was measured. Fluorescence measurements of the sample were carried out with excitation at 312 nm.

2.3.3. Superoxide radical test. In this test, nitro blue tetrazolium chloride (NBT) of $1 \times 10^{-5} \text{ M}$ was dissolved into 100 ml of DI water and stirred [33]. During the stirring, 6 mg of catalyst was added and this was further stirred for 1 h. The irradiation time and sample collection after irradiation was similar to that of hydroxyl radical test. UV–vis absorption measurements were carried out with a commercial spectrophotometer (Shimadzu, UV3101PC).

3. Results and discussion

Figure 1 shows the steps involved in the synthesis of Au@GQD-GCN by citrate reduction method. For the decoration of Au NPs over the hybrid, GQD-GCN is dispersed in aqueous Au³⁺ solution. The solution is kept in stirring condition for distribution of Au³⁺ ions over the GQD-GCN. The solution is heated to boiling and then TSC is added. TSC reduces Au³⁺ to metallic Au⁰ on the surface of GQD-GCN. The completion of the reaction is monitored by the appearance of purple-white coloured solution. In figure 1, we have shown that Au (shown by purple ball) NPs are associated with GQD (blue ball) and GCN in Au@GQD-GCN. There are, however, possible locations on GCN nanosheets where Au NPs remain in contact with GCN without being in contact with GQD. However, for an understanding of the plasmonic hybrid formation we have considered in the schematic the locations where there is possibility of Au NPs being in contact with GQD and GCN.

Figure 2(a) shows the XRD pattern of pristine GQD, GCN, GQD-GCN and Au@GQD-GCN. The single intense diffraction peak in GQD at $2\theta = 26.3^\circ$ can be indexed to (002) crystallographic plane of GQD [34]. The (002) diffraction peak at $2\theta = 27.5^\circ$ in GCN is attributable to the

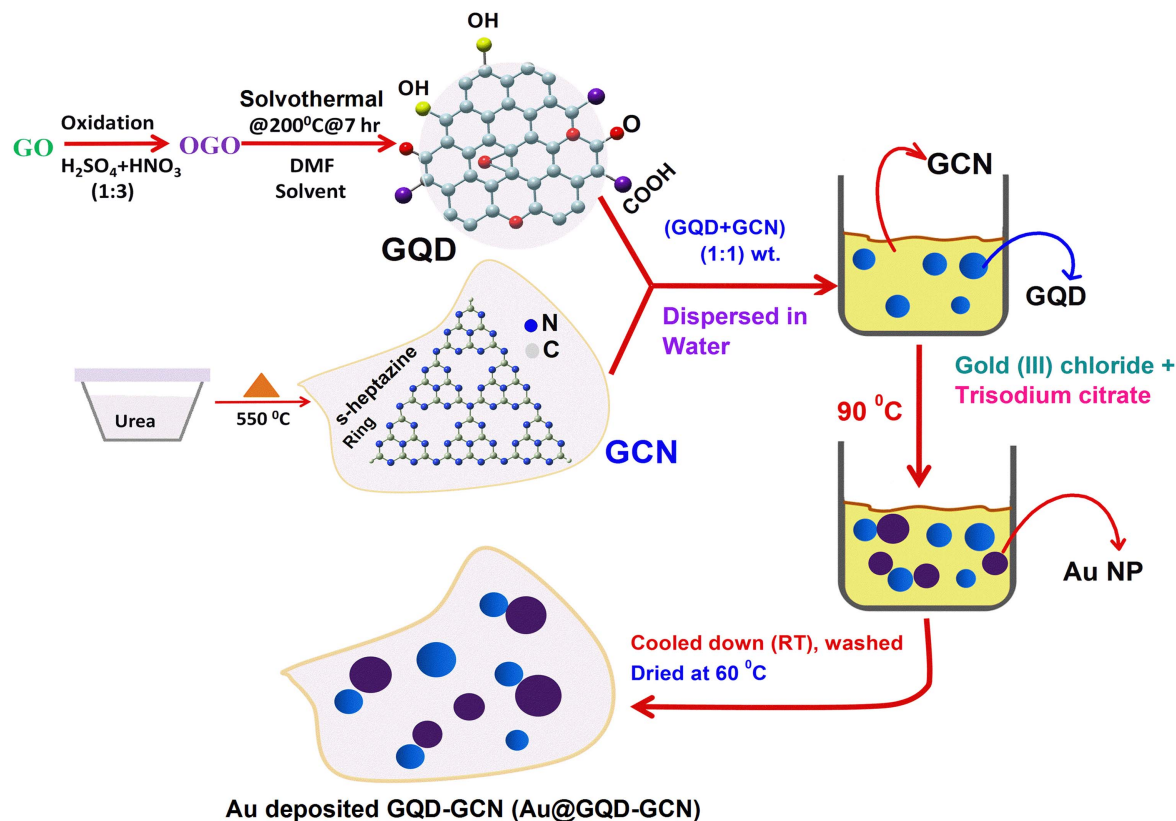


Figure 1. Schematic showing the synthesis of GQDs from oxidized graphene oxide (OGO), GCN nanosheets from urea and *in situ* deposition of Au NPs (0.5 mM) over hybrid nanosystem of GQD-GCN by a citrate reduction method.

interlayer spacing of GCN nanosheets [35]. In the GQD-GCN hybrid system, the major peak corresponds to GQD and the shoulder peak corresponds to (002) plane of GCN. Along with the diffraction peaks of GQD and GCN, the reflection lines of face-centred-cubic (fcc) Au is clearly observed in the XRD pattern of Au@GQD-GCN. The diffraction peaks at 38.2° , 44.4° and 64.4° are in agreement with the fcc phase structure of Au (JCPDS 04-0784) [36]. Figures 2(b)–(f) display the TEM images of GCN, GQD, Au NP, and Au@GQD-GCN, respectively. GCN appears as buckled porous nanosheets, as seen in figure 2(b). TEM image of GQD (figure 2(c)) confirms the presence of quantum dots of average diameter 5.2 nm (see inset of figure 2(c)), whereas Au NPs (figure 2(d)) have an average diameter of 10.7 nm (inset of figure 2(d)). Figures 2(e)–(f) show the TEM images of Au@GQD-GCN hybrid system. From the figures it is apparent that most of the Au NPs are present over the surface of the hybrid nanosystems of GQD-GCN. It is apparent from figure 2(e) that all the GQD-GCN sites are not decorated with Au NPs. Only about 50% sites are decorated with Au NPs and some of the Au NPs are lying isolated. For a clear view of the interface between GQDs and Au NPs, a high resolution TEM image of the plasmonic hybrid nanosystem was taken (see figure 2(f)). The lattice planes of Au NPs are indicated with an arrow. The NPs enclosed by the dotted line corresponds to GQD (matched with particle size distribution), which is attached to the Au NPs. Note that the lattice planes are not clear in the region where Au and GQD are overlapped. We

speculate that the GQDs are attached to Au NPs as well as distributed over GCN nanosheets. For further confirmation of the presence of Au in the hybrid system, we performed elemental mapping of Au@GQD-GCN. Figure 2(g) shows the FESEM image of Au NPs decorated GQD-GCN. Figures 2(h)–(k) shows the elemental mapping of C, N, O and Au. The different contrast mappings of C, N, O and Au show their distribution in the hybrid photocatalyst. Presence of O $K\alpha$ reveals that the hybrid system contains many oxygenated functional groups attached at the edges/in-plane sites on GQD.

Figure 3(a) shows the Raman spectra of GQD, GQD-GCN and Au@GQD-GCN for an excitation wavelength of 488 nm. Raman spectra of different samples display the characteristic G band ($\sim 1580\text{ cm}^{-1}$) of GQD, which is associated with in-plane phonon vibration of sp^2 carbon atoms with E_{2g} symmetry. The D band at 1350 cm^{-1} with A_{1g} symmetry becomes activated in the presence of defects and involves transverse optical phonons around K -point of Brillouin zones [37–39]. Weak Raman band at 2730 cm^{-1} is the 2D band, which is the overtone of D-band. This band is resulted from the double resonance transition producing two phonons of opposite momentum [39]. The relative intensity of disorder induced D band to crystalline G band (I_D/I_G) is nearly 1 in all the samples, which signifies that the prepared GQDs contain functional groups and unsaturated carbon on the edges [40]. There is a slight modification of Raman bands of GQD in the hybrid GQD-GCN and Au@GQD-GCN.

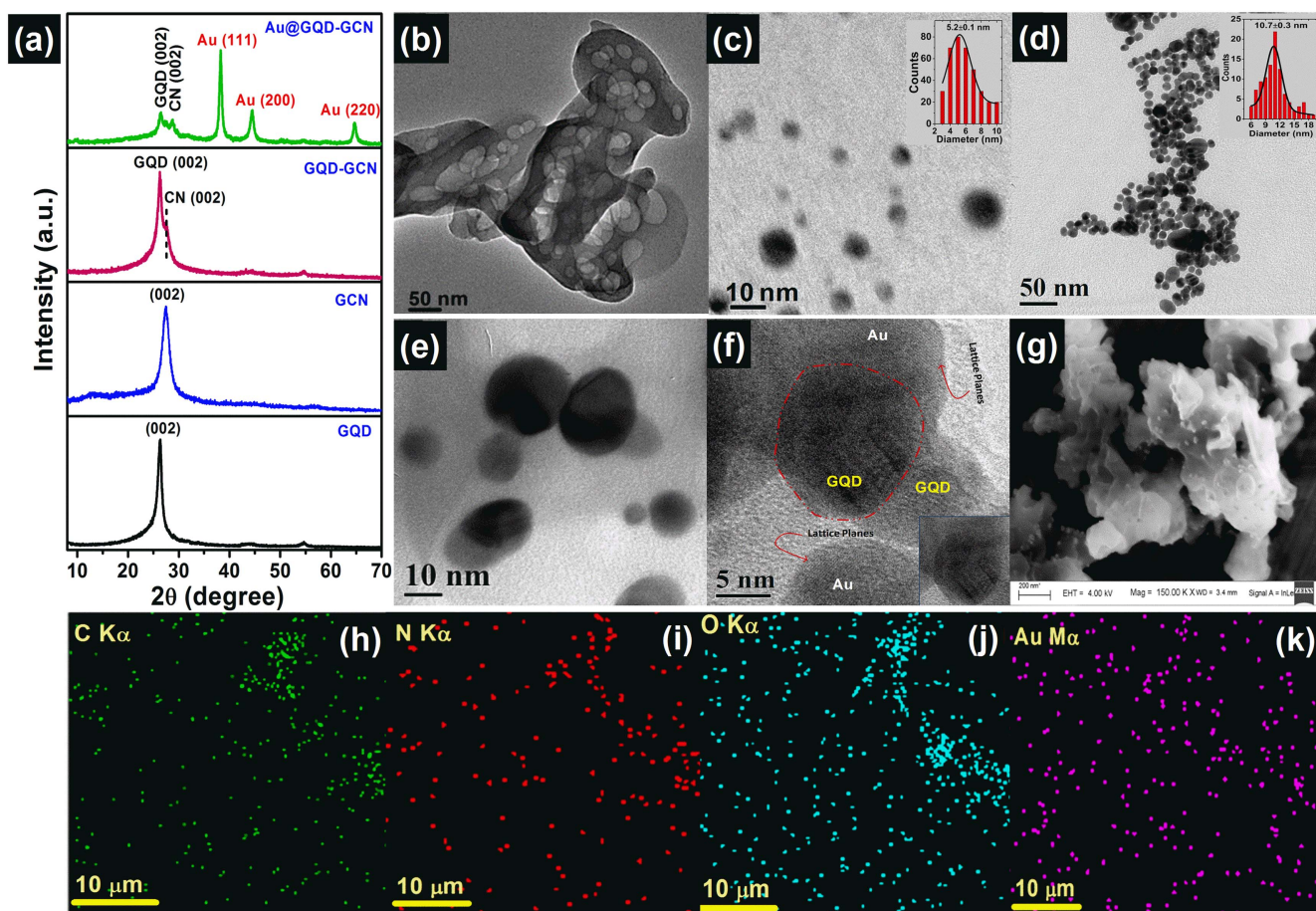


Figure 2. (a) XRD pattern of GQD, GCN, GQD-GCN and Au@GQD-GCN. TEM images of (b) GCN (c) GQD (d) Au NPs and (e)–(f) Au@GQD-GCN hybrid system. (g) FESEM image of Au@GQD-GCN. Elemental mapping for (h) C (i) N (j) O and (k) Au.

Next, we analyse the Raman spectra of the same systems with 514.5 nm laser excitation (figure 3(b)). There is a significant change in the intensity of D and G bands with a change in excitation wavelength. From figure 3(b), it is apparent that the G and 2D band intensity is enhanced due to the presence of Au NPs. This might be caused by the Au plasmon induced surface enhanced Raman scattering (SERS). The enhancement factor (EF) is determined by the ratio of intensity, $EF = I_{Au}/I_{Pristine}$ for both G and 2D bands [41]. It is found that the G band intensity is enhanced by a factor of 1.3 and the 2D band intensity is enhanced by a factor of 7 after Au deposition. Interestingly, the incident radiation of $\lambda = 514.5$ nm is close to the SPR band of Au NPs seen at 532 nm (discussed later). Because of the close proximity of the resonant bands of Au NPs with the excitation laser wavelength, there is an enhancement of electromagnetic field intensity at the Au NPs and GQD-GCN interface and this strong electromagnetic coupling enhances SERS effect [41]. Note that there is a decrease in D band intensity in GQD-GCN after Au deposition. This might be due to the reduction in the numbers of unsaturated carbon sites due to the attachment of Au on these sites through Au–C bond formation.

Figure 3(c) displays the FTIR spectra of the plasmonic hybrid system and their associates. GQD shows a strong band

at 3463 cm^{-1} . This is due to the stretching vibration of edge states -OH moiety. The vibration at 1569 cm^{-1} is linked with the aromatic C=C bond and the associated minor shoulder peak at 1410 cm^{-1} can be assigned to C–H bending vibration mode [42–44]. The weak bands at 1638 cm^{-1} and 1081 cm^{-1} are assigned to C=O stretching mode in carboxylic acid and C–O stretching peak in epoxide, respectively [40, 45]. GCN shows several strong absorption bands. The band at 812 cm^{-1} is the breathing mode of aromatic ring (*s*-heptazine) of GCN [35, 46]. The weak absorption band at 887 cm^{-1} is attributed to C, N out of plane rocking mode in *s*-heptazine unit [47]. The broad absorption band covering $3000\text{--}3600\text{ cm}^{-1}$ is a contribution from N–H stretching vibration of any uncondensed amine groups [48]. The absorption bands at 1238, 1323, 1410, 1462, 1572 and 1636 cm^{-1} are typically associated with symmetric, asymmetric stretching and bending vibrations of different C–N (or C=N) bonds in the heptazine derived repeating units and correspond to either trigonal C–N (–C)–C (full condensation) or bridging C–NH–C units (partial condensation) [35, 47, 48]. In GQD-GCN, the bands corresponding to C=O, C=C and C–O bonds of GQD are submerged with *s*-heptazine ring vibrational mode in C_3N_4 in the range $1100\text{--}1600\text{ cm}^{-1}$. No change is observed in the FTIR spectrum of GQD-GCN after Au deposition.

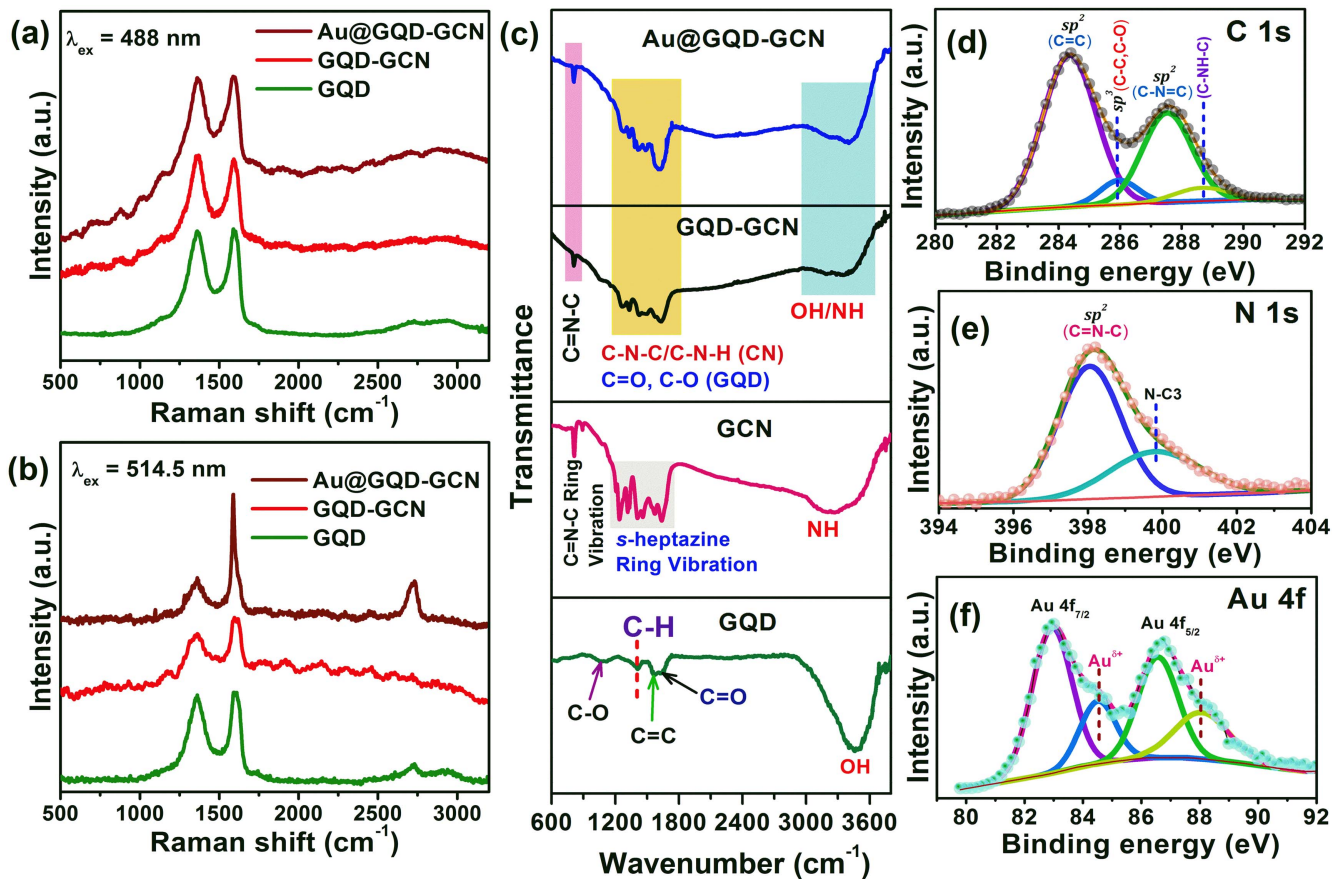


Figure 3. Raman spectra of GQD, GQD-GCN and Au@GQD-GCN with excitation wavelength (a) 488 nm and (b) 514.5 nm. (c) FTIR spectra of GQD, GCN, GQD-GCN and Au@GQD-GCN. XPS spectra of (d) C 1s (e) N 1s and (f) Au 4f in Au@GQD-GCN.

The chemical composition of Au@GQD-GCN is characterized by XPS. Figure 3(d) shows the C1s spectrum, which is deconvoluted into four components with each peak having the contribution from different forms of carbon in GQD and GCN. The four components of C1s XPS of Au@GQD-GCN appear at 284.4, 286.0, 287.5 and 288.6 eV, respectively. The intense peak at 284.4 eV is attributed to sp^2 C=C bonding of graphitic domain [14, 49]. The second intense peak at 287.5 eV can be attributed to aromatic sp^2 C=N=C linkages in the aromatic ring of g-C₃N₄ in hybrid [50, 51]. The peak at 286.0 eV has origin due to the presence of sp^3 carbon attached with functional groups or disordered states, such as C-C, C-O (ether), surface states, etc [26, 52]. One more peak appears at 288.7 eV which might be associated with C-NH-C linkages formed by the attachment of hydrogen on the bridging N atom coordinating the aromatic rings in the hybrid system.

Figure 3(e) displays the deconvoluted N 1s spectrum of the hybrid system. The peak at 398.0 eV is due to aromatic sp^2 (C=N-C) bonding in the s-heptazine ring, and the peak at 399.4 eV is assigned to bridging N atom (N-C3) in GCN [51]. XPS spectrum of Au 4f has two strong doublets at 83.0 eV (Au 4f_{7/2}) and 86.6 eV (Au 4f_{5/2}). These peaks signify the presence of metallic Au⁰ in the hybrid system (figure 3(f)) [53–55]. There is a negative shift (−0.8 eV) of the doublets of Au in the hybrid system with respect to the positions reported for pristine metallic Au, which are at

83.8 eV and 87.4 eV respectively [55, 56]. The negative shift of the XPS peak is identified with electron transfer occurring from GQD-GCN to Au NPs [54, 55]. There are two shoulder peaks in Au 4f spectrum which are at the higher binding energy sides of the strong doublets. These peaks are at 84.5 eV and 88.1 eV, and attributed to the presence of cationic gold species (Au^{δ+}). An appearance of charged species might be due to the formation of Au-C bonding at the interface of Au and GQD-GCN [57].

Figure 4(a) shows the optical absorption spectra of the samples under investigation. GQD exhibits two absorption bands at 268 nm and 332 nm, respectively. The maximal absorption at 268 nm can be ascribed to $\pi-\pi^*$ transition of sp^2 C=C skeletal framework. The shoulder absorption at 332 nm is owing to the $n-\pi^*$ transitions and involves non-bonding electrons present on oxygen (C=O or C-O) of the attached functional groups (epoxy, carboxy, etc) at carbon edges [52, 58]. GCN has a strong absorption peak at 370 nm. This peak is attributed to $n-\pi^*$ electronic transition involving lone pair electrons on nitrogen 2p orbital [35, 49]. GQD-GCN contains an absorption at 256 nm due to $\pi-\pi^*$ transition of sp^2 carbon (C=C) of GQD, two small humps at 326 and 387 nm and an absorption tail extended to the visible region. The humps at 326 and 387 nm correspond to $n-\pi^*$ transition involving oxygen lone pair electrons in the case of GQD and nitrogen lone pair electrons in GCN, respectively. The

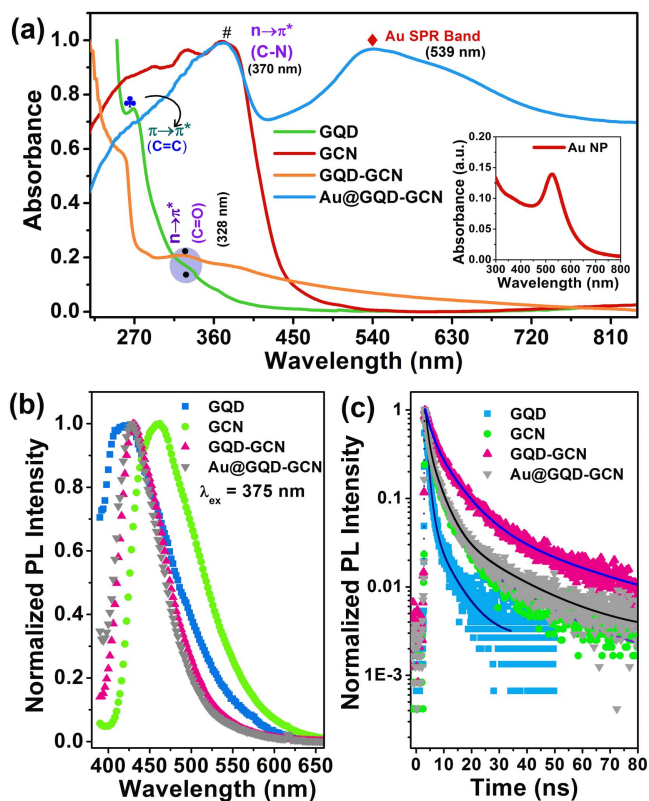


Figure 4. (a) Absorption spectra of GQD, GCN, GQD-GCN and Au@GQD-GCN. Inset shows the absorption spectrum Au NPs. (b) Steady state PL spectra of GQD, GCN, GQD-GCN and Au@GQD-GCN excited at 375 nm. (c) TRPL spectra of the samples with 375 nm excitation.

absorption tail appears because of the presence of disordered states (oxygenated states, carbon or nitrogen vacancies) at the interface of GQD-GCN. The absorption spectrum of Au@GQD-GCN has two significant absorption bands. The higher energy band correspond to $n-\pi^*$ transition in GCN (at 371 nm) and the lower energy band refers to the SPR band (at 539 nm) of embedded Au NPs [59]. The expected UV absorption bands of GQDs are merged with the broad absorption spectrum of the plasmonic hybrid system. For the pristine Au NPs, a narrow SPR band is observed at 527 nm (inset of figure 4(a)). In the hybrid system, there is a red shift in the SPR band by 12 nm. The changes in the dielectric media surrounding the Au NPs in the hybrid system might have resulted in the red shift of the absorption band [59].

Figure 4(b) displays the steady-state PL spectra of plasmonic Au NPs decorated GQD-GCN and their associates. The samples show blue-green emission on excitation at 375 nm. The most intense emission appears in the blue region. The emission spectrum of GQD shows a peak at 423 nm and an emission tail extended to the visible region. In conformity with the available literature reports, we infer that the PL in GQD is due to the presence of oxygenated functional groups ($-\text{OH}$, COOH , $\text{C}=\text{O}$, etc) and edge states (armchair and zig-zag edges) localized in the $\pi-\pi^*$ energy gap of GQD [52, 60]. GCN displays a strong emission at 460 nm. Unlike GQD, the emissions in GCN are due to various

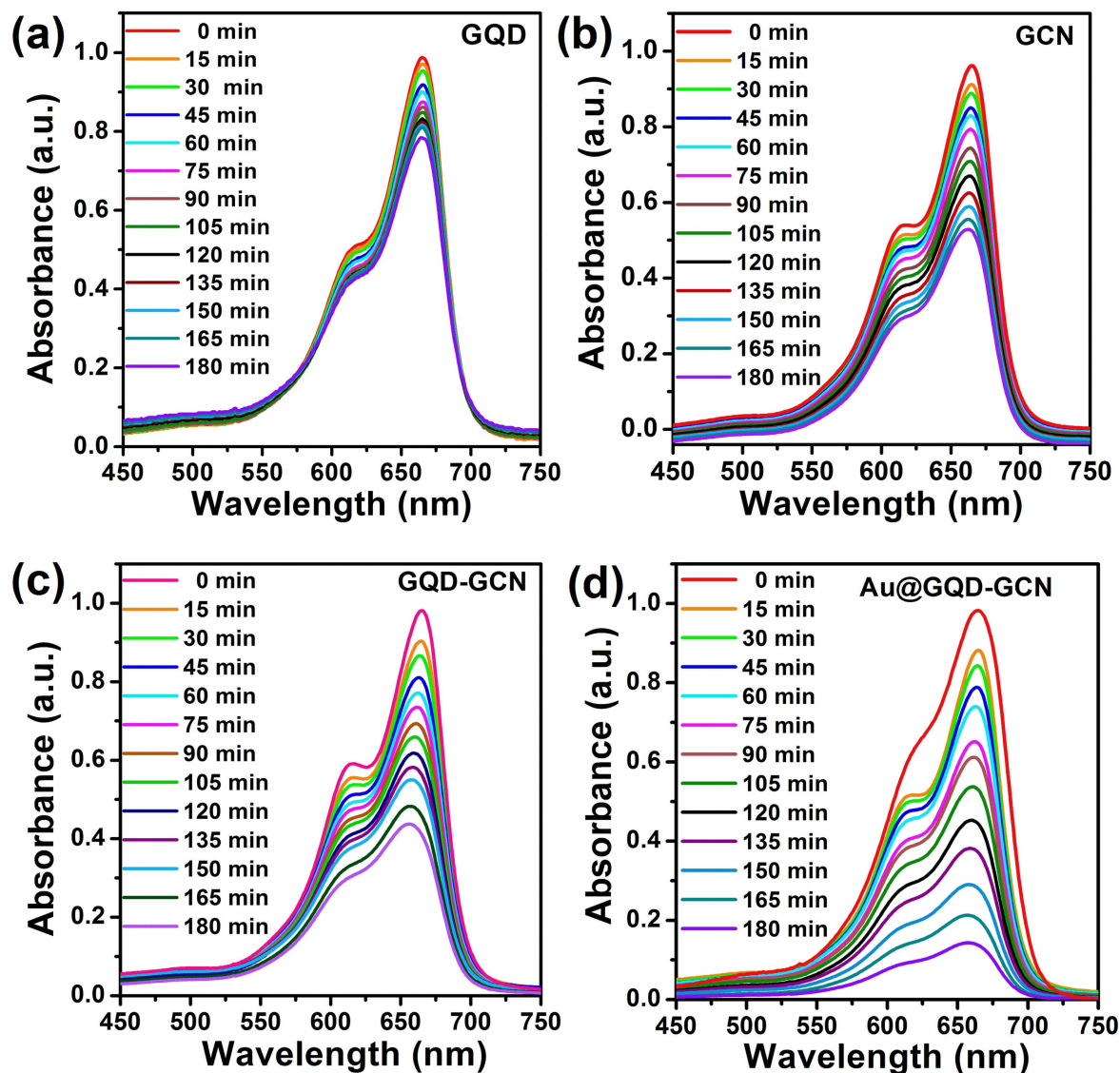
electronic transitions in the *s*-heptazine ring. Band states of GCN consist of sp^2 ($\text{C}=\text{N}$) π bond, sp^3 ($\text{C}-\text{N}$) σ bond and lone pair (LP, n) electrons present on bridging N atom in *s*-heptazine ring [61]. On photoexcitation, electrons are excited to the highest energy states in the conduction band and then finally relax to the lowest occupied molecular orbital, which is the $\text{C } 2p \pi^*$ state. From π^* states, the electrons undergo $\pi^*-\pi$, π^*-n transition giving rise to the various emission peaks. Emissions at longer wavelength are mostly due to the presence of intra-gap electronic states in GCN [62]. The hybrid GQD-GCN displays maximum emission at 432 nm and the emission spectrum looks similar to that of GQD. There is, however, no noticeable change in the emission profile of GQD-GCN after Au deposition.

In order to understand the carrier relaxation dynamics in GQD-GCN, Au@GQD-GCN and their associates, we performed the TRPL measurement. The samples are excited at 375 nm (figure 4(c)). Lifetime of the charge carriers and their relative abundances are obtained after tri-exponential fitting of the spectra. The results are listed in table 1. The shortest lifetime ($\tau_1 \sim 0.46$ ns) in GQD can be associated with $\pi^*-\pi$ transition of sp^2 bonded core carbon. Various sources might contribute to the extended lifetimes (τ_2 and τ_3) in GQD. These include presence of armchair or zig-zag edges, defect states and functional groups [52, 60, 63]. GCN has a short carrier lifetime of 0.86 ns (τ_1) which is due to π^*-n transition. Long components 4.23 ns (τ_2) and 21.45 ns (τ_3) can be associated with the presence of intra-gap states in GCN. These intra-band gap states form both shallow and deep trap states in the band gap of GCN. The carriers are relaxed for a sufficiently longer period in those traps before they undergo recombination. The average carrier lifetimes (τ_{av}) in GQD and GCN are 4.3 ns and 16.3 ns, respectively. The hybrid GQD-GCN has the longest average carrier lifetime of 20.8 ns. The interface developed between GQD and GCN could be responsible for the prolonged charge carrier lifetime in GQD-GCN. Note that, after Au decoration, the average carrier lifetime of the hybrid system reduces to 16.2 ns. The reduction in the carrier lifetime is due to enhanced charge transfer interaction in plasmonic hybrid system. This result is in conformity with the earlier reports in plasmonic based hybrid nanosystems [64, 65]. The charge transportation occurs from hybrid to Au NPs where Au acts as electron reservoir.

MB is considered as the model organic compound to study the PC activities of the different catalytic systems under consideration. Figure 5 shows the UV-vis absorption spectra of MB irradiated for different times in the presence of catalysts GQD, GCN, GQD-GCN and Au@GQD-GCN. The absorption maximum of MB at 665 nm gradually decreases in intensity as irradiation continues. The reduction in intensity is most prominent when irradiation is performed in the presence of Au@GQD-GCN. Figure 6(a) shows the photodegradation of MB as a function of irradiation time. It is seen that in the absence of catalyst, MB molecule itself is inactive to undergo self-degradation under visible light and only 12% degradation occurs after 180 min of irradiation. When GQD is added to the MB solution and photoactivity is evaluated, only 22% MB degradation is recorded. GCN, however, shows superior PC

Table 1. Carrier lifetime components (τ_1 , τ_2 , τ_3), their relative abundances (A_1 , A_2 , A_3) and the average carrier lifetime (τ_{av}) for GQD, GCN, GQD-GCN and Au@GQD-GCN, as determined from TRPL analysis.

Sample	τ_1 (ns) ($A_1\%$)	τ_2 (ns) ($A_2\%$)	τ_3 (ns) ($A_3\%$)	τ_{Av} (ns)
GQD	0.46 (30.4)	1.42 (39.8)	6.73 (29.8)	4.3
GCN	0.86 (26.8)	4.23 (48.2)	21.45 (25.0)	16.3
GQD-GCN	1.60 (13.0)	6.66 (51.6)	26.37 (35.4)	20.8
Au@GQD-GCN	0.82 (21.3)	3.87 (49.0)	20.6 (29.7)	16.2

$$\tau_{av} = \sum_{i=1}^3 \frac{A_i \tau_i^2}{A_i \tau_i}$$
**Figure 5.** Absorption spectra of MB taken after visible light irradiation for 0–180 min. Irradiation was performed in presence of catalysts (a) GQD (b) GCN (c) GQD-GCN and (d) Au@GQD-GCN with catalyst loading of 6 mg and initial dye concentration of 8 mg l^{-1} .

activity than GQD and a 48% MB degradation is achieved. GQD-GCN hybrid shows 54% degradation of MB. In our earlier study, we have shown that Au NPs itself is not useful in MB degradation [29]. However, present results demonstrate that when Au NPs are anchored on the surface of GQD-GCN, the PC activity of the later is enhanced and 86% MB degradation has been achieved over the irradiation time of

180 min. The kinetics of the PC reactions follows a pseudo first order process expressed by $\ln(C_t/C_0) = -kt$, where k is the reaction rate constant obtained from the slope of the linear plot (figure 6(b)). In order to understand how Au deposition might influence the PC activity of pristine GQD and GCN, we have performed PC measurements of Au-GQD and Au-GCN (figure 6(c)). Photodegradation of MB enhances for both

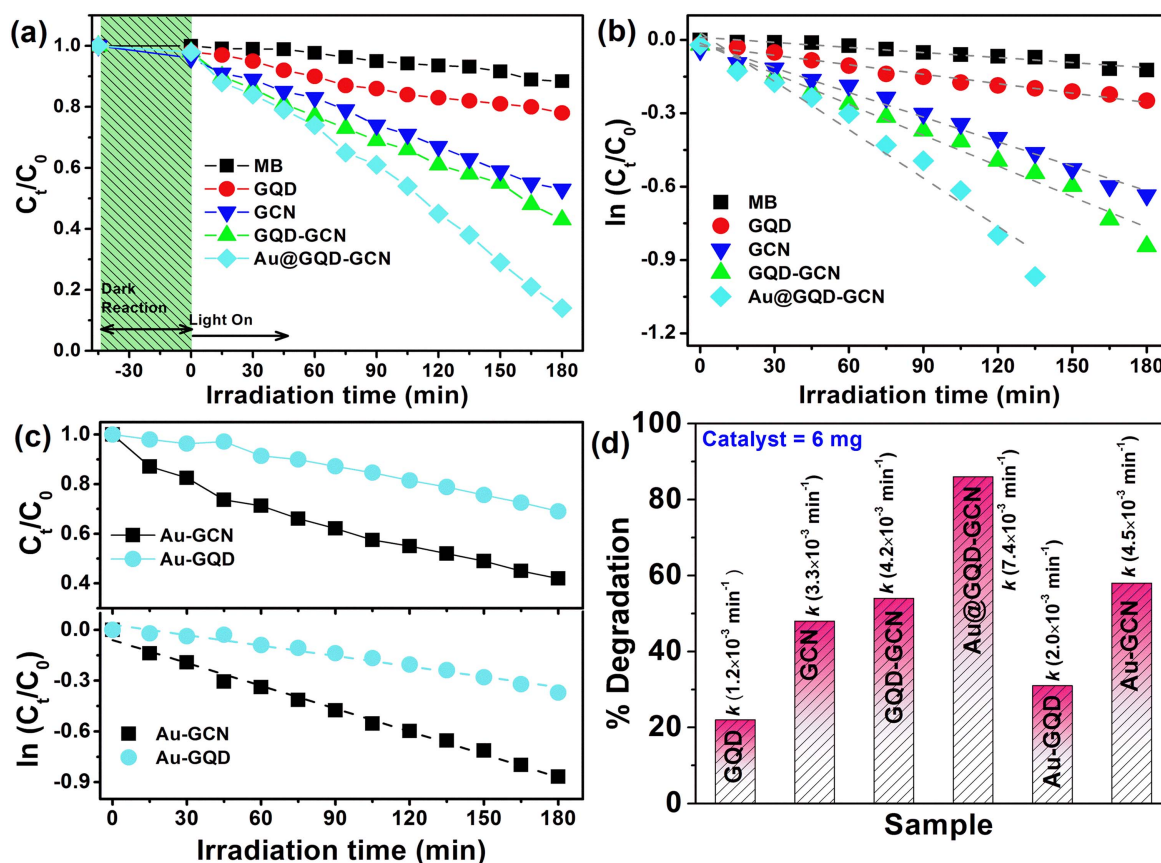


Figure 6. (a) Photodegradation of MB in presence of different catalysts. (b) Pseudo first order rate kinetics of MB photodecomposition. (c) Photodegradation and reaction kinetics of MB decomposition in presence of catalysts Au-GQD and Au-GCN. (d) Percent degradation and rate constant values for different samples in MB degradation.

GQD and GCN when these catalysts are decorated with Au NP. We have reported MB degradation of 58% and 31% in presence of Au-GCN and Au-GQD, respectively. Figure 6(d) clearly reveals that the rate kinetics shown by Au@GQD-GCN is nearly 6 fold higher than that of GQD and 2 fold higher than GCN and GQD-GCN.

PC reaction in aqueous solution is initiated by hydroxyl ($\cdot\text{OH}$) and superoxide radicals ($\text{O}_2^{\cdot-}$). In order to know their presence in irradiated MB solution and to confirm their participation in photocatalysis, we have performed TA detection test and NBT test [66, 67]. Figures 7(a), (b) shows TA and NBT test for detection of $\cdot\text{OH}$ and $\text{O}_2^{\cdot-}$ radicals. There is an irreversible reaction between TA and $\cdot\text{OH}$ radical to form 2-hydroxy TA (figure 7(c)), which shows strong PL at 424 nm under UV excitation (312 nm). The PL intensity directly measures the amount of $\cdot\text{OH}$ present in the solution. Increase in PL intensity with irradiation time reflects the production of $\cdot\text{OH}$ radicals during the PC reaction. Other primary and secondary radicals, such as $\cdot\text{H}$, HO_2 and H_2O_2 do not significantly affect the induced PL [66]. Presence of $\text{O}_2^{\cdot-}$ is verified with the help of UV-vis spectroscopy. NBT is used for the detection of $\text{O}_2^{\cdot-}$ radical in solution. NBT shows an absorption maximum at 255 nm. NBT is very sensitive to electron donor and therefore, in presence of $\text{O}_2^{\cdot-}$ NBT is reduced to its formazon form producing its characteristic purple colour (figure 7(d)) [67]. If there are large

concentrations of $\text{O}_2^{\cdot-}$ radicals in the solution, the absorption peak intensity will eventually decrease with irradiation time. However, $\cdot\text{OH}$ shows better response to TA test than $\text{O}_2^{\cdot-}$ to NBT test confirming that $\cdot\text{OH}$ could be the major species in photocatalysis.

Based on the visible light PC results of GQD, GCN, GQD-GCN and Au@GQD-GCN, we may highlight the following points to explain the mechanism of their PC activities.

3.1. GQD and GCN

Despite the presence of reactive oxygenated functional groups, GQD exhibits very poor PC activity. As revealed by the TRPL analysis, the oxygenated functional groups in GQD act as carrier recombination centres. Therefore, available numbers of free carriers are less able to take part in the photocatalysis. Moreover, its poor absorption in the visible region could be another factor behind its low PC activity. Unlike GQD, GCN appears to be a better photocatalyst. The better PC activity of GCN can be attributed to its extended visible absorption and prolonged carrier lifetime.

3.2. GQD-GCN

TRPL analysis of the sample shows a longer carrier lifetime implying a superior interfacial carrier separation. Presence of sufficient numbers of free electrons and holes at the interface

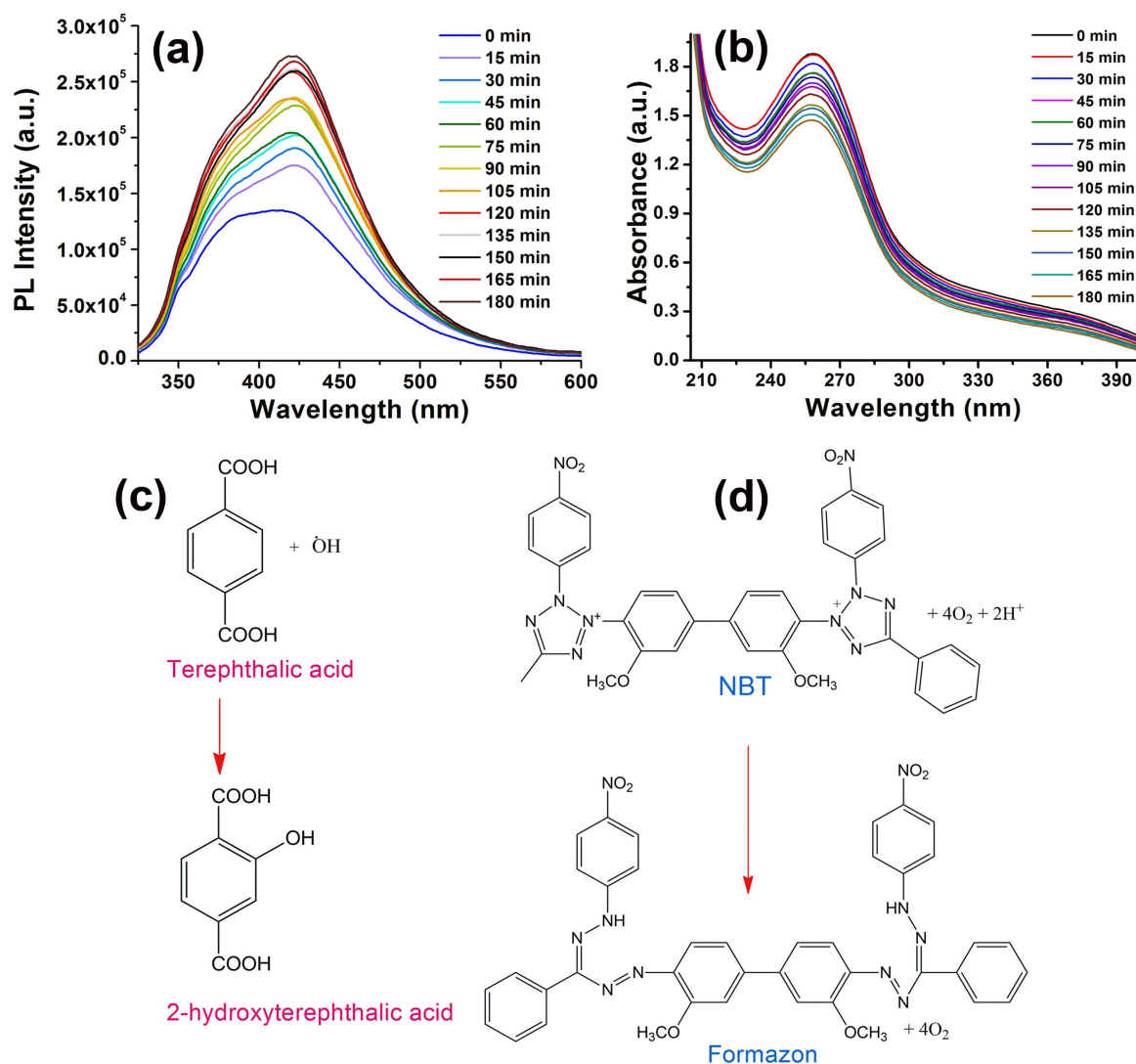


Figure 7. Identification of hydroxyl (OH) and superoxide (O₂⁻) radicals in photoirradiated aqueous MB solution with (a) terephthalic acid (TA) and (b) nitro blue tetrazolium chloride (NBT) test. Tests are performed in presence of Au@GQD-GCN. Schematic of reaction showing conversion of (c) terephthalic acid to 2-hydroxy terephthalic acid and (d) NBT to formazon.

can readily interact with adsorbed MB molecules and could speed up the photodegradation of MB. The hybrid system also shows broad absorption tail extended to ~ 720 nm in the visible region. Extended visible absorption and efficient interfacial charge separation are likely to be the key factors behind the improved PC activity in GQD-GCN.

3.3. Au-GQD, Au-GCN and Au@GQD-GCN

It is observed that after the deposition of Au NPs, the PC activities of GQD, GCN and GQD-GCN hybrids are enhanced. Au NPs may act as electron traps and might enable hole separation on the material/substrate where it is attached. Further, because of the SPR effect, plasmonic Au NPs will enhance the localized electric field surrounding the Au NPs [27, 28]. This enhancement of optical field at the proximity of the attached semiconductor will provide facile electron-hole separation. The above explanations can be illustrated with the help of a schematic, as shown in figure 8(a). When Au is

deposited over GQD-GCN, the Au NPs may get attached with both GCN and GQD. Because of SPR effect, Au NPs are able to concentrate high light intensity (optical field enhancement) at the interface of GCN-Au-GQD. This will trigger photoexcitation of electrons in both GQD and GCN. Photoexcitation is followed by charge transfer from hybrid system to Au NPs. However, in case of Au-GCN and Au-GQD, the deposited Au NPs will trigger photoexcitation on GQD or GCN. Therefore, the optical field enhancement for carrier excitation and separation are expected to be weaker in Au-GCN or Au-GQD as compared to those in Au@GQD-GCN. Plasmon induced MB degradation is reported in ternary layered hybrid systems of Au-C₃N₄-Graphene [68]. In this study, Xue *et al* observed 97% degradation of MB for irradiation time of 240 min with 100 mg catalyst in 10 mg l⁻¹ solution of MB. In the present study, we have achieved 86% degradation of MB with 6 mg catalyst in 8 mg l⁻¹ MB solution under an irradiation time of 180 min. Based on the comparative results, we believe that the present 0D-2D

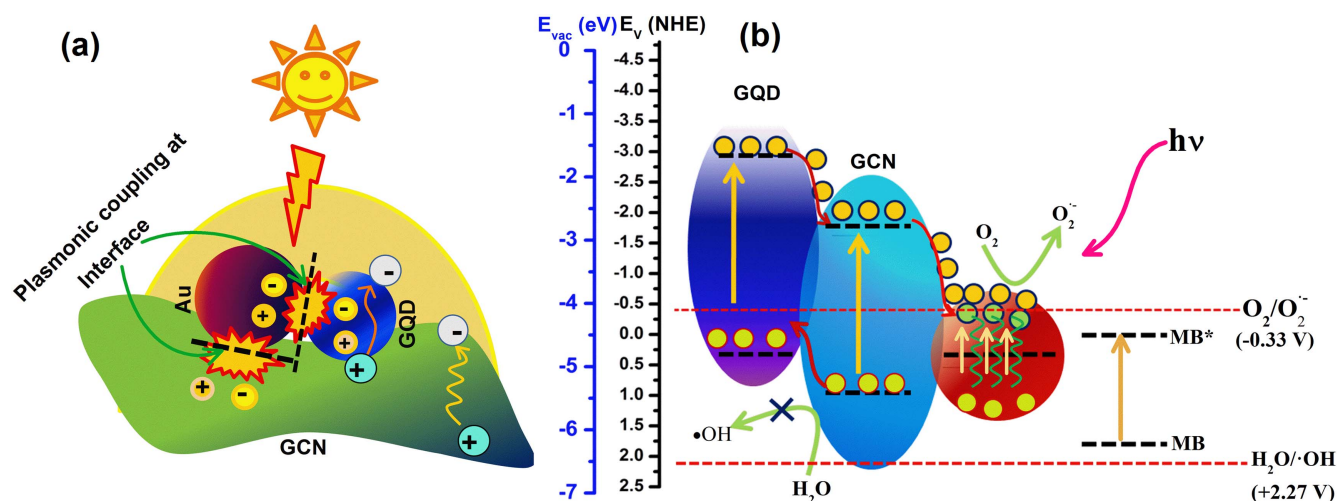
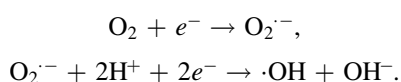


Figure 8. (a) Schematic of SPR absorption under visible light and photoexcitation of carriers at the interface between Au-GQD-GCN in the plasmonic hybrid photocatalyst. (b) Schematic of band structure of plasmonic hybrid nanosystem with generation of radical species.

hybrid system of GQD-GCN decorated with Au NPs perform as an efficient visible light photocatalyst.

Note that Au@GQD-GCN shows better PC activity than the other catalysts. In order to understand the mechanism for the enhanced PC activity in Au@GQD-GCN, we need to understand the charge separation, charge transfer and charge accumulation process in the plasmonic hybrid. Carrier separation and charge transfer depends on the band structure of the hybrid. We have drawn a band diagram of the plasmonic hybrid system based on the available literature reports on the band structure of GQD, GCN, Au and MB [69–75]. In conformity with the literature reports, the conduction band and valence band position of GQD is drawn at -1.57 and -4.8 eV, for GCN these positions are -2.82 and -5.47 eV, Au NPs have a work function of -4.75 eV, and for MB the band positions are at -4.55 and -6.26 eV versus vacuum scale. The relation between redox potentials versus normal hydrogen electrode and work functions versus vacuum scale is given by $E = -4.5 \text{ eV} - E_{\text{NHE}} (\text{V})$ [72]. The standard redox potential of $\text{O}_2/\text{O}_2^{\cdot-}$ and $\text{H}_2\text{O}/\cdot\text{OH}$ are -0.33 V and $+2.27$ V versus normal hydrogen electrode. The schematic band diagram is shown in figure 8(b). It is evident from the figure that valence band holes cannot oxidize H_2O to $\cdot\text{OH}$. We might speculate an indirect way for hydroxyl radical formation. Superoxide radicals are unstable in solution and are prone to form stable hydroxyl radical in solution. Our TA test also showed evidences for higher amount of hydroxyl radical in solution. The formation of hydroxyl radical through superoxide radical formation can be explained with the following reaction steps [35].



One important issue with the visible light absorbing dye molecule is its self-sensitization effect. Under the visible light illumination, the MB molecule undergoes photoexcitation to a

higher energy state. However, from the position of conduction band of MB, it is clear that transfer of electrons from photoexcited MB^* to GQD or GCN is not feasible. Electron transfer from MB^* to Au, however, might take place. However, our previous report shows that Au NPs itself does not show any appreciable photoactivity in MB degradation [29]. Therefore, the photodegradation of MB is initiated only in presence of plasmonic hybrid catalyst with negligible possibility of self-sensitized photodegradation. Therefore, the PC processes can be summarized as follows. Under photoexcitation of visible light, GQD-GCN, which absorbs mostly in the near visible region, can be excited by visible light $\lambda < 460$ nm. However, longer wavelength ($\lambda > 530$ nm) light exposure stimulates SPR absorption in Au NPs. The plasmon excitation will generate large enhancement of optical field in the vicinity of Au NPs at the interface with GQD-GCN (see figure 8(a)). This optical field will trigger energetic electron generation in the neighbourhood of GQD-GCN. Photoexcited carriers, generated in the hybrid as a result of plasmonic absorption, will migrate to Au NPs and participate in PC reaction. Electrons in Au forms $\text{O}_2^{\cdot-}$ by interacting with surface adsorbed O_2 . In solution $\text{O}_2^{\cdot-}$ are transformed to $\cdot\text{OH}$ ions, which initiate photodegradation of MB.

4. Conclusion

We have shown that plasmonic Au NPs have a profound effect in the enhancement of PC activity of 0D–2D (GQD-GCN) hybrid systems. The presence of oxygenated functional groups on GQD (unlike pure graphene) and the presence of interlinked *s*-heptazine chains and bridging N in GCN sheets have a beneficial effect on the charge carrier separation, leading to moderate PC activity. In the hybrid system, electron transfer occurs from GQD to GCN nanosheets and the presence of Au NPs enhance the charge transfer efficiency

from the GQD-GCN to Au by the intermediary Au–C bond at the interface. Plasmonic excitation not only generates sufficient surface electrons on Au but also photoexcites charge carriers at the GQD-GCN interface, in the vicinity of Au NPs. Because of the plasmonic effect, large enhancement in PC activity was observed in Au@GQD-GCN over other catalysts under the illumination of visible light.

Acknowledgments

BC would like to acknowledge the Department of Science and Technology (DST, Govt. of India) for providing the DST Inspire faculty award to carry out this work. The authors would like to thank the Central Instrumentation Facility (CIF), IIT Guwahati for providing various characterisation facilities. We thank Prof M Fujii, Kobe University, for the XPS measurement.

References

- [1] Djuricic A B, Leung Y H and Ching Ng A M 2014 Strategies for improving the efficiency of semiconductor metal oxide photocatalysis *Mater. Horiz.* **1** 400
- [2] Serpone N and Emeline A V 2012 Semiconductor photocatalysis past, present, and future outlook *J. Phys. Chem. Lett.* **3** 673
- [3] Choudhury B, Bayan S, Choudhury A and Chakraborty P 2016 Narrowing of band gap and effective charge carrier separation in defective TiO₂ nanotube *J. Colloid Interface Sci.* **465** 1
- [4] Hisatomi T, Kubota J and Domen K 2014 Recent advances in semiconductors for photocatalytic and photoelectrochemical water splitting *Chem. Soc. Rev.* **43** 7520
- [5] Choi J, Park H and Hoffmann M R 2010 Effects of single metal-ion doping on the visible-light photoreactivity of TiO₂ *J. Phys. Chem. C* **114** 783
- [6] Marchall R and Wang L 2014 Non-metal doping of transition metal oxides for visible-light photocatalysis *Catal. Today* **225** 111
- [7] Paul S, Chetri P, Choudhury B, Ahmed G A and Choudhury A 2015 Enhanced visible light photocatalytic activity of Gadolinium doped nanocrystalline titania: an experimental and theoretical study *J. Colloid Interface Sci.* **439** 54
- [8] Choi W, Termin A and Hoffmann M R 1994 The role of metal ion dopants in quantum-sized TiO₂: correlation between photoreactivity and charge carrier recombination dynamics *J. Phys. Chem.* **98** 13669
- [9] Luo B, Liu G and Wang L 2016 Recent advances in 2D materials for photocatalysis *Nanoscale* **8** 6904
- [10] Raccichini R, Varzi A, Passerini S and Scrosati B 2015 The role of graphene for electrochemical energy storage *Nat. Mater.* **14** 271
- [11] Varghese S S, Lonkar S, Singh K K, Swaminathan S and Abdala A 2015 Recent advances in graphene based gas sensors *Sensors Actuators B* **218** 160
- [12] Zhang N, Yang M Q, Liu S, Sun Y and Xu Y J 2015 Waltzing with the versatile platform of graphene to synthesize composite photocatalysts *Chem. Rev.* **115** 10307
- [13] Ong W J, Tan L L, Ng Y H, Yong S T and Chai S P 2016 Graphitic carbon nitride (g-C₃N₄)-based photocatalysts for artificial photosynthesis and environmental remediation: are we a step closer to achieving sustainability? *Chem. Rev.* **116** 7159
- [14] Chen J, Zhang Y, Zhang M, Yao B, Li Y, Huang L, Li C and Shi G 2016 Water-enhanced oxidation of graphite to graphene oxide with controlled species of oxygenated groups *Chem. Sci.* **7** 1874
- [15] Ramirez K B, Diaz C, Icaza M, Hernandez A and Santos C 2015 Photocatalytic activity in phenol removal of water from graphite and graphene oxides: effect of degassing and chemical oxidation in the synthesis process *J. Chem.* **2015** 1
- [16] Ramirez K B, Diaz C, Herrera M, Hernandez A, Reyna R and Santos C 2015 4-chlorophenol removal from water using graphite and graphene oxides as photocatalysts *J. Environ. Health Sci. Eng.* **13** 1
- [17] Shan X, Guo X, Yin Y, Miao Y and Dong H 2017 Surface modification of graphene oxide by goethite with enhanced tylosin photocatalytic activity under visible light irradiation *Colloids Surf. A* **520** 420
- [18] Wang Y, Wang X and Antonietti M 2012 Polymeric graphitic carbon nitride as a heterogeneous organocatalyst: from photochemistry to multipurpose catalysis to sustainable chemistry *Angew. Chem., Int. Ed.* **51** 68
- [19] Chen C, Cai W, Long M, Zhou B, Wu Y, Wu D and Feng Y 2010 Synthesis of visible-light responsive graphene oxide/TiO₂ composites with p/n heterojunction *ACS Nano* **4** 6425
- [20] Hao R, Wang G, Tang H, Sun L, Xu C and Han D 2016 Template-free preparation of macro/mesoporous g-C₃N₄/TiO₂ heterojunction photocatalysts with enhanced visible light photocatalytic activity *Appl. Catalysis B* **187** 47
- [21] Lai S K, Xie C, Teng K S, Li Y, Tan F, Yan F and Lau S P 2016 Polymeric carbon nitride nanosheets/graphene hybrid phototransistors with high responsivity phototransistors with high responsivity *Adv. Opt. Mater.* **4** 555
- [22] Zhao H, Chen S, Quan X, Yu H and Zhao H 2016 Integration of microfiltration and visible light-driven photocatalysis on g-C₃N₄ nanosheet/reduced graphene oxide membrane for enhanced water treatment *Appl. Catalysis B* **194** 134
- [23] Liao G, Chen S, Quan X, Yu H and Zhao H 2012 Graphene oxide modified g-C₃N₄ hybrid with enhanced photocatalytic capability under visible light irradiation *J. Mater. Chem.* **22** 2721
- [24] Wan W, Yu S, Dong F, Zhang Q and Zhou Y 2016 Efficient C₃N₄/graphene oxide macroscopic aerogel visible-light photocatalyst *J. Mater. Chem. A* **4** 7823
- [25] Ma Z, Sa R, Li Q and Wu K 2016 Interfacial electronic structure and charge transfer of hybrid graphene quantum dot and graphitic carbon nitride nanocomposites: insights into high efficiency for photocatalytic solar water splitting *Phys. Chem. Chem. Phys.* **18** 1050
- [26] Zou J P, Wang L C, Luo J, Nie Y C, Xing Q J, Luo X B, Du H M, Luo S L and Suib S L 2016 Synthesis and efficient visible light photocatalytic H₂ evolution of a metal-free g-C₃N₄/graphene quantum dots hybrid photocatalyst *Appl. Catalysis B* **193** 103
- [27] Zhang X, Chen Y L, Liu R S and Tsai D P 2013 Plasmonic photocatalysis *Rep. Prog. Phys.* **76** 046401
- [28] Boriskina S V, Ghasemi H and Chen G 2013 Plasmonic materials for energy: from physics to applications *Mater Today* **16** 375
- [29] Biroju R K, Choudhury B and Giri P K 2016 Plasmon-enhanced visible light photocatalysis by defect engineered CVD graphene and graphene oxide physically functionalized with Au nanoparticles *Catal. Sci. Tech.* **6** 7101
- [30] Chen J, Yao B, Li C and Shi G 2013 An improved Hummers method for eco-friendly synthesis of graphene oxide *Carbon* **64** 225

- [31] Lee M J, Lim S H, Ha J M and Choi S M 2016 Green synthesis of high-purity mesoporous gold sponges using self-assembly of gold nanoparticles induced by thiolated poly(ethylene glycol) *Langmuir* **32** 5937
- [32] Bakar S A, Byzinski G and Ribeiro C 2016 Synergistic effect on the photocatalytic activity of N doped TiO₂ nanorods synthesized by novel route with exposed (110) facet *J. Alloys Compd.* **666** 38
- [33] Ye L, Liu J, Jiang Z, Peng T and Zan L 2013 Facets coupling of BiOBr-g-C₃N₄ composite photocatalyst for enhanced visible light driven photocatalytic activity *Appl. Catalysis B* **142–143** 1
- [34] Zhang Z, Zhang J, Chen N and Qu L 2012 Graphene quantum dots: an emerging material for energy-related applications and beyond *Energy Environ. Sci.* **5** 8869
- [35] Choudhury B and Giri P K 2016 Isotype heterostructure of bulk and nanosheets of graphitic carbon nitride for efficient visible light photodegradation of methylene blue *RSC Adv.* **6** 24976
- [36] Li C C, Chen L B, Li Q H and Wang T H 2012 Seed-free, aqueous synthesis of gold nanowires *CrystEngComm* **14** 7549
- [37] Tuinstra F and Koenig J L 1970 Raman spectrum of graphite *J. Chem. Phys.* **53** 1126
- [38] Kim S, Shin D H, Kim C O, Kang S S, Joo S S, Choi S H, Hwang S W and Sone C 2013 Size dependence of Raman scattering from graphene quantum dots: interplay between shape and thickness *Appl. Phys. Lett.* **102** 053108
- [39] Ferrari A C and Robertson J 2000 Interpretation of Raman spectra of disordered and amorphous carbon *Phys. Rev. B* **61** 14095
- [40] Suzuki N et al 2016 Chiral graphene quantum dot *ACS Nano* **10** 1744
- [41] Sun H B, Wu J, Zhu J J, Pan D F, Wang G H and Wan J G 2015 Great SERS Raman scattering in hybrids consisting of graphene and silver nanoparticles with larger particle size *Appl. Phys. Lett.* **106** 211603
- [42] Wang L et al 2014 Gram scale synthesis of single crystalline grapheme QD with superior optical properties *Nat. Commun.* **5** 1
- [43] Tang L et al 2012 Deep ultraviolet photoluminescence of water-soluble self-passivated graphene quantum dots *ACS Nano* **6** 5102
- [44] Wang L et al 2014 Common origin of green luminescence in carbon nanodots and graphene quantum dots *ACS Nano* **8** 2541
- [45] Jin S H, Kim D H, Jun G H, Hong S H and Jeon S 2013 Tuning the PL of GQD through the charge transfer effect of functional groups *ACS Nano* **7** 1239
- [46] She X, Xu H, Xu Y, Yan J, Xia J, Xu L, Song Y, Jiang Y, Zhang Q and Li H 2014 Exfoliated graphene-like carbon nitride in organic solvents: enhanced photocatalytic activity and highly selective and sensitive sensor for the detection of trace amounts of Cu²⁺ *J. Mater. Chem. A* **2** 2563
- [47] Zheng W, Wong N B, Zhou G, Liang X, Li J and Tian A 2004 Theoretical study of tri-s-triazine and some of its derivatives *New J. Chem.* **28** 275
- [48] Niu P, Liu G and Cheng H M 2012 Nitrogen vacancy-promoted photocatalytic activity of graphitic carbon nitride *J. Phys. Chem. C* **116** 11013
- [49] Park S, An J, Piner R D, Jung I, Yang D, Velamakanani A, Nguyen S T and Ruoff R S 2008 Aqueous suspension and characterization of chemically modified graphene sheets *Chem. Mater.* **20** 6592
- [50] Li X, Hartley G, Ward A J, Young P A, Masters A F and Maschmeyer T 2015 Hydrogen defects in graphitic carbon nitride nanosheets for improved photocatalytic H₂ evolution *J. Phys. Chem. C* **119** 14938
- [51] Zhou Z, Shen Y, Li Y, Liu A, Liu S and Zhang Y 2015 Chemically cleavage of layered carbon nitride with enhanced PL performances and photoconduction *ACS Nano* **9** 12480
- [52] Rajender G and Giri P K 2016 Formation mechanism of graphene quantum dots and their edge state conversion probed by photoluminescence and Raman spectroscopy *J. Mater. Chem. C* **4** 10852
- [53] Klyushin A Y, Greiner M T, Huang X, Lunkenbein T, Li X, Timpe O, Friedrich M, Hävecker M, Gericke A K and Schlögl R 2016 Is nanostructuring sufficient to get catalytically active Au *ACS Catal.* **6** 3372
- [54] Li J, Liu C and Liu Y 2012 Au/grapheme hydrogel: synthesis, characterisation and its use for catalytic reduction of 4 nitrophenol *J. Mater. Chem.* **22** 8426
- [55] Wang R, Wu Z, Wang G, Qin Z, Chen C, Dong M, Zhu H, Fan W and Wang J 2015 Highly active Au–Pd nanoparticles supported on 3D grapheme carbon nanotube hybrid for selective oxidation of methanol to methyl formate *RSC Adv.* **5** 44835
- [56] Wagner C D, Riggs W M, Davis L E and Moulder J F 1979 *Handbook of X-ray Electron Spectroscopy* (Minnesota, MN: Perkin-Elmer Corp.)
- [57] Yang E, Chou H, Tsumura S and Nagatsu M 2016 Surface properties of plasma functionalized graphite encapsulated Au NPs prepared by direct current arc discharge *J. Phys. D: Appl. Phys.* **49** 185304
- [58] Sarkar S, Gandla D, Venkatesh Y, Bangal P R, Ghosh S, Yang Y and Misra S 2016 Graphene quantum dots from graphite by liquid exfoliation showing excitation independent emission, fluorescence upconversion and delayed fluorescence *Phys. Chem. Chem. Phys.* **18** 21278
- [59] Jiang R, Li B, Fang C and Wang J 2014 Metal/semiconductor hybrid nanostructures for plasmon-enhanced applications *Adv. Mater.* **26** 5274
- [60] Zhu S, Shao J, Song Y, Zhao X, Du J, Wang L, Wang H, Zhang K, Zhang J and Yang B 2015 Investigating the surface state of graphene quantum dots *Nanoscale* **7** 7927
- [61] Bian J, Li J, Kalytchuk S, Wang Y, Li Q, Lau T C, Niehaus T A, Rogach A L and Zhang R Q 2015 Efficient emission facilitated by multiple energy level transitions in uniform graphitic carbon nitride films deposited by thermal vapor condensation *ChemPhysChem.* **16** 954
- [62] Wu P, Wang J, Zhao J, Guo L and Osterloh F E 2014 Structural defects in g-CN limit visible light driven H₂ evolution and photovoltage *J. Mater. Chem. A* **2** 20338
- [63] Lin L and Zhang S 2012 Creating high yield water soluble luminescent graphene quantum dots via exfoliating and disintegrating carbon nanotubes and graphite flakes *Chem. Commun.* **48** 10177
- [64] Khoa N T, Kim S W, Yoo D H, Cho S, Kim E J and Hahn S H 2015 Fabrication of Au/Graphene/ZnO nanoparticles assembled hollow spheres with effective photoinduced charge transfer for photocatalysis *ACS Appl. Mater. Interfaces* **7** 3524
- [65] Lee J, Shim H S, Lee M, Song J K and Lee D 2011 Size-controlled electron transfer and photocatalytic activity of ZnO–Au nano-particle composites *J. Phys. Chem. Lett.* **2** 2840
- [66] Nosaka Y, Komori S, Yawata K, Hirakawa T and Nosaka A Y 2003 Photocatalytic OH radical formation in TiO₂ aqueous suspension studied by several detection method *Phys. Chem. Chem. Phys.* **5** 4731
- [67] Hayyan M, Hashim M A and Al Nashef I M 2016 Superoxide ion: generation and chemical applications *Chem. Rev.* **116** 3029
- [68] Xue J, Ma S, Zhou Y and Wang Q 2015 Au-loaded porous graphitic C₃N₄/graphene layered composite as a ternary plasmonic photocatalyst and its visible-light photocatalytic performance *RSC Adv.* **5** 88249

- [69] Lu Q, Zhang Y and Liu S 2015 Graphene quantum dots enhanced photocatalytic activity of zinc porphyrin toward degradation of methylene blue under visible light irradiation *J. Mater. Chem. A* **3** 8552
- [70] Ritter K A and Lyding J W 2009 The influence of edge structure on the electronic properties of grapheme quantum dots and nanoribbons *Nat. Mater.* **8** 235
- [71] Wu H Z, Liu L M and Zhao S J 2014 The effect of water on the structural, electronic and photocatalysis properties of graphitic carbon nitride *Phys. Chem. Chem. Phys.* **16** 3299
- [72] Xiong Z, Zhang L L, Ma J and Zha X S 2010 Photocatalytic degradation of dyes over grapheme gold composite *Chem. Commun.* **46** 6099
- [73] Chu S, Wang Y, Guo Y, Feng J, Wang C, Luo W, Fan X and Zou Z 2013 Band structure engineering of carbon nitride: in search of a polymer photocatalyst with high photooxidation property *ACS Catalysis* **3** 912
- [74] Li H J, Sun B W, Sui L, Qian D J and Chen M 2015 Preparation of water-dispersible porous g-C₃N₄ with improved photocatalytic activity by chemical oxidation *Phys. Chem. Chem. Phys.* **17** 3309
- [75] Shen J S, Yu T, Xie J W and Jiang Y B 2009 Photoluminescence of CdTe nanocrystals modulated by methylene blue and DNA. A label-free luminescent signaling nanohybrid platform *Phys. Chem. Chem. Phys.* **11** 5062